

Original article

An energy stable numerical scheme for simulating compressible gas flow in poroelastic media

Huangxin Chen¹, Yuxiang Chen^{2*}, Jisheng Kou^{3*}

¹*School of Mathematical Sciences and Fujian Provincial Key Laboratory on Mathematical Modeling and High Performance Scientific Computing, Xiamen University, Fujian 361005, P. R. China*

²*School of Mathematical Sciences and Fujian Provincial Key Laboratory on Mathematical Modeling and High Performance Scientific Computing, Xiamen University, Fujian 361005, P. R. China*

³*School of Civil Engineering, Shaoxing University, Zhejiang 312000, P. R. China*

Keywords:

Gas flow in porous media
energy stability
mass conservation
thermodynamic consistency

Cited as:

Chen, H., Chen, Y., Kou, J. An energy stable numerical scheme for simulating compressible gas flow in poroelastic media. *Computational Energy Science*, 2024, 1(2): 86-101.
<https://doi.org/10.46690/compes.2024.02.03>

Abstract:

An efficient numerical method is developed to simulate compressible gas flow in porous media coupled with compressible rocks. Since the model is strongly nonlinear and fully coupled, it is challenging to design numerical methods that satisfy certain energy dissipation laws. We employ a stabilization method to design a time semi-discrete scheme that is weakly nonlinear and satisfies the energy dissipation law. Using the conservative finite element methods with the upwind strategy, we construct the fully discretized approximation that satisfies the laws of mass conservation and energy dissipation. The simulation results are provided to exhibit the features of the method as proved in theory.

1. Introduction

Numerical modeling of gas flow through porous media is of particular importance in contemporary energy industries, including environmental pollution, petroleum engineering, and geotechnical engineering (Firoozabadi, 1999; Chen et al., 2006). Therefore, numerical simulation of gas flow in porous media has attracted the attention of more and more researchers (Guo et al., 2013; Polívka and Mikyška, 2014; El-Amin et al., 2018). Numerical methods in literature mainly focus on gas behavior when it flows through porous materials and analyze important properties like pressure distribution, and gas molar density distribution. The most commonly used governing equations describing the complex interaction between the gas phase and the porous matrix are Darcy's law, mass conservation equation, and realistic equations of state to characterize the gas compressibility (Chen et al., 2006; Kou

et al., 2022). Solid compressibility is another important factor affecting gas flow in porous media (Chen et al., 2006; Xu et al., 2018; Du et al., 2021; Kou et al., 2022). Appropriate mathematical models and constitutive relations should be used to describe the mechanical properties of the solid phase. In this paper, we use the model of Biot's consolidation of poroelasticity to explain rock volume changes.

Energy dissipation is a crucial factor in accurately predicting the behavior of compressible gas flow in porous media. The energy dissipation law is straightforwardly deduced from the second law of thermodynamics, which governs energy behavior and the nature of physical processes. Adherence to the energy dissipation law is essential for achieving valid and stable numerical solutions in simulations of gas flow through porous media (Chen et al., 2006; Lebon et al., 2008; Kou and Sun, 2018, 2018a;).

Numerical simulations that do not properly account for

energy dissipation laws are prone to producing inaccurate predictions of gas flow behavior. The development of thermodynamically consistent models has also attracted the attention of researchers such as phase-field modeling (Lowengrub and Truskinovsky, 1998; Abels et al., 2012; Shen et al., 2013; Aki et al., 2014; Guo et al., 2017; Shokrpour Roudbari et al., 2018; Zhu et al., 2019) and compressible multiphase flow (Qiao and Sun, 2014; Kou and Sun, 2015, 2018). To well simulate a thermodynamically consistent model, it is necessary to design numerical algorithms that satisfy energy dissipation. Various numerical methods have been explored to address the Helmholtz free energy, such as the stabilization methods (Xu and Tang, 2006), the convex splitting approach (Eyre et al., 1998), the exponential time-differencing methods (Du et al., 2021), the invariant energy quadratization (IEQ) approach (Yang and Ju, 2017; Yang et al., 2017a) and the scalar auxiliary variable (SAV) approach (Shen et al., 2018; Shen et al., 2019). The IEQ and SAV approaches can lead to linear and straightforward-to-implement time-discrete schemes that are also energy-stable. However, the discrete energies generated by IEQ and SAV approaches are different from the original energy. In Kou et al. (2020, 2022), an energy factorization (EF) technique is introduced as a means of constructing discrete schemes that are computationally efficient, linear in nature, and retain the energy dissipation characteristics of the original problem. In this paper, we adopt a novel stabilization approach proposed in Kou et al. (2023), which can maintain the original energy function and get a numerically stable linear scheme. Local mass conservation is also an important factor in the numerical modeling of compressible gas flow in porous media. Mass-conserving numerical approaches have been the subject of considerable attention and focus (Yue et al., 2007; Aland and Voigt, 2012; Ding and Yuan, 2014; Wang et al., 2015; Guo et al., 2017; Chen et al., 2019; Kou et al., 2020). This paper adopts the discontinuous Galerkin (DG) method to solve the poroelasticity model, and the mixed finite element method with an upwind technique is used for the fluid field solution. Based on these methods, we introduce a spatial discretized approximation that can preserve the mass conservation.

The paper is organized as follows. In Section 2, we present the formulation of a gas flow in a porous media model that incorporates rock compressibility effects. In Sections 3 and 4, we propose the semi-discretized and fully discretized formulations of the method as well as present the corresponding theoretical investigation. In Section 5, some numerical results will be given to demonstrate the good performance of the method.

2. Mathematical model

In this section, we briefly introduce the gas flow model that incorporates rock compressibility.

2.1 Model equations

The gas flow model with compressible rocks (Chen et al., 2024) reads:

$$\nabla \cdot \boldsymbol{\sigma}(\mathbf{u}_s, p) = 0, \quad \text{in } \Omega_t =: \Omega \times (0, t), \quad (1a)$$

$$\boldsymbol{\sigma}(\mathbf{u}_s, p) = \boldsymbol{\sigma}_e(\mathbf{u}_s) - \alpha p \mathbf{I}, \quad \text{in } \Omega_t, \quad (1b)$$

$$\frac{\partial(c\phi)}{\partial t} + \nabla \cdot (c\mathbf{v}_f) = 0, \quad \text{in } \Omega_t, \quad (1c)$$

$$\mathbf{v}_f = -c\lambda(\phi)\nabla\mu, \quad \text{in } \Omega_t, \quad (1d)$$

$$p = \mu c - f, \quad \text{in } \Omega_t, \quad (1e)$$

$$\frac{\partial\phi}{\partial t} = \left(\frac{1}{N}\right)\partial_t p + \alpha\partial_t \nabla \cdot \mathbf{u}_s, \quad \text{in } \Omega_t, \quad (1f)$$

where $\boldsymbol{\sigma}_e(\mathbf{u}_s) = 2\eta\boldsymbol{\varepsilon}(\mathbf{u}_s) + \gamma\text{div}(\mathbf{u}_s)\mathbf{I}$ represents the elastic stress tensor, \mathbf{I} is the unit tensor, $\boldsymbol{\varepsilon}(\mathbf{u}_s) := \frac{1}{2}(\nabla\mathbf{u}_s + \nabla\mathbf{u}_s^T)$ is the strain tensor and \mathbf{u}_s is the displacement of solid, η and γ are the Lamé constants, c is the molar density, \mathbf{v}_f represents the velocity of gas, p stands for the pressure of gas, α is the Biot constant, N reflects the rock compression and ϕ represents the porosity.

The homogeneous Neumann-type boundary conditions read:

$$\boldsymbol{\sigma}(\mathbf{u}_s, p) \cdot \mathbf{n} = 0, \quad \text{on } \partial\Omega, \quad (2a)$$

$$\mathbf{v}_f \cdot \mathbf{n} = 0, \quad \text{on } \partial\Omega, \quad (2b)$$

where \mathbf{n} is the unit outer normal of the boundary $\partial\Omega$.

The Helmholtz energy density $f(c)$ determined by the equation of state (Peng and Robinson, 1976) for constant temperature T is described as below:

$$f(c) = f_{ide}(c) + f_{rep}(c) + f_{att}(c), \quad (3a)$$

$$f_{ide}(c) = cRT \ln(c), \quad (3b)$$

$$f_{rep}(c) = -cRT \ln(1 - \beta c), \quad (3c)$$

$$f_{att}(c) = \frac{b(T)c}{2\sqrt{2}\beta} \ln\left(\frac{1 + (1 - \sqrt{2})\beta c}{1 + (1 + \sqrt{2})\beta c}\right), \quad (3d)$$

where R represents the universal gas constant. The relevant parameters can be found in the literature, for instance, (Kou et al., 2023). The chemical potential energy $\mu(c)$ can be expressed as:

$$\mu(c) = f'(c).$$

The total free energy is defined as (cf. Chen et al., 2024):

$$E(t) = \int_{\Omega} \left(\phi f(c) + \frac{1}{2} \boldsymbol{\sigma}_e(\mathbf{u}_s) : \boldsymbol{\varepsilon}(\mathbf{u}_s) + \frac{1}{2N} |p|^2 \right) dx. \quad (4)$$

Theorem 2.1. Assume that the boundary condition 2 holds, then the model 1 obeys an energy dissipation law, which can be expressed as:

$$\frac{\partial E(t)}{\partial t} = - \int_{\Omega} \lambda(\phi) |c \nabla \mu(c)|^2 dx \leq 0.$$

A detailed proof of Theorem 2.1 can be found in (Chen et al., 2024).

3. Semi-discretized formulation

The section establishes a time semi-discrete scheme using a stabilization-based approach.

3.1 Semi-implicit formulation

We use $\tau = t_{n+1} - t_n$ to represent the time step size. Let B^n represent the value of B discretized at time t_n and let $D_\tau B^{n+1} := \frac{B^{n+1} - B^n}{\tau}$, where $B = \mathbf{u}_s, \phi, p, c, E$. We denote by (\cdot, \cdot) and $\|\cdot\|_{L^2(\Omega)}$ the standard inner product and norm of $L^2(\Omega)$.

This paper employs a stabilization approach. The stabilized discrete chemical potential, involving the stabilization parameter θ , is defined as (Kou et al., 2023):

$$\mu^{n+1} = \mu(c^n) + \theta RT \frac{c^{n+1} - c^n}{c^n(1 - \beta c^n)^2}. \quad (5)$$

We introduce the semi-implicit scheme:

$$-\nabla \cdot \sigma_e(\mathbf{u}_s^{n+1}) + \alpha \nabla p^{n+1} = 0, \quad (6a)$$

$$D_\tau(\phi^{n+1} c^{n+1}) + \nabla \cdot (\mathbf{v}_f^{n+1} c^n) = 0, \quad (6b)$$

$$\mathbf{v}_f^{n+1} = -\lambda(\phi^n) c^n \nabla \mu^{n+1}, \quad (6c)$$

$$p^{n+1} = c^n \mu^{n+1} - f(c^n), \quad (6d)$$

$$D_\tau \phi^{n+1} = \frac{1}{N} D_\tau p^{n+1} + \alpha \nabla \cdot D_\tau \mathbf{u}_s^{n+1}. \quad (6e)$$

Theorem 3.1. Assume that $0 < \varepsilon \leq c^n \leq \frac{1}{\beta} - \varepsilon$, where ε is a given small constant. If the stabilization parameter θ satisfies:

$$\theta \geq \frac{N_{\max} c^n (1 - \beta c^n)^2}{2RT}, \quad (7)$$

where N_{\max} is the upper bound of $|f''(c)|$ in $(\varepsilon, \frac{1}{\beta} - \varepsilon)$. Then the scheme 6 adheres to an energy decreasing law:

$$E^{n+1} \leq E^n,$$

where

$$E^n = \int_{\Omega} \left(\phi^n f(c^n) + \frac{1}{2} \sigma_e(\mathbf{u}_s^n) : \varepsilon(\mathbf{u}_s^n) + \frac{1}{2N} |p^n|^2 \right) dx. \quad (8)$$

Proof. By the Taylor expansion, we have

$$f(c^{n+1}) - f(c^n) = \mu(c^n)(c^{n+1} - c^n) + \frac{f''(\xi)}{2}(c^{n+1} - c^n)^2.$$

By Eq. 7 and considering the stabilized chemical potential Eq. 5, we obtain

$$\begin{aligned} & f(c^{n+1}) - f(c^n) \\ &= \mu^{n+1}(c^{n+1} - c^n) + \left(\frac{f''(\xi)}{2} - \frac{\theta RT}{c^n(1 - \beta c^n)^2} \right) (c^{n+1} - c^n)^2 \\ &\leq \mu^{n+1}(c^{n+1} - c^n). \end{aligned} \quad (9)$$

Due to Eq. 9, we get

$$\begin{aligned} & \phi^{n+1} f(c^{n+1}) - \phi^n f(c^n) \\ &\leq \mu^{n+1} \phi^{n+1} (c^{n+1} - c^n) + f(c^n) (\phi^{n+1} - \phi^n) \\ &= \mu^{n+1} (\phi^{n+1} c^{n+1} - \phi^n c^n) - p^{n+1} (\phi^{n+1} - \phi^n). \end{aligned} \quad (10)$$

Taking the L^2 inner product of Eqs. 6a and 6e with $D_\tau \mathbf{u}_s^{n+1}$ and p^{n+1} and adding Eqs. 6a and 6e together, we get

$$\begin{aligned} & 2\eta(\varepsilon(\mathbf{u}_s^{n+1}), \varepsilon(D_\tau \mathbf{u}_s^{n+1})) + \gamma(\nabla \cdot \mathbf{u}_s^{n+1}, \nabla \cdot (D_\tau \mathbf{u}_s^{n+1})) \\ &+ \frac{1}{N} (D_\tau p^{n+1}, p^{n+1}) - (D_\tau \phi^{n+1}, p^{n+1}) = 0. \end{aligned} \quad (11)$$

The first, second, and third terms on the left-hand side of Eq. 11 can be rewritten as:

$$\begin{aligned} & 2\eta(\varepsilon(\mathbf{u}_s^{n+1}), \varepsilon(D_\tau \mathbf{u}_s^{n+1})) \\ &= \eta \tau \|D_\tau \varepsilon(\mathbf{u}_s^{n+1})\|_{L^2(\Omega)}^2 + \eta D_\tau \|\varepsilon(\mathbf{u}_s^{n+1})\|_{L^2(\Omega)}^2, \end{aligned} \quad (12)$$

$$\begin{aligned} & \gamma(\nabla \cdot \mathbf{u}_s^{n+1}, \nabla \cdot (D_\tau \mathbf{u}_s^{n+1})) = \frac{\gamma \tau}{2} \|\nabla \cdot D_\tau \mathbf{u}_s^{n+1}\|_{L^2(\Omega)}^2 \\ &+ \frac{\gamma}{2} D_\tau \|\nabla \cdot \mathbf{u}_s^{n+1}\|_{L^2(\Omega)}^2, \end{aligned} \quad (13)$$

$$\frac{\tau}{N} (D_\tau p^{n+1}, p^{n+1}) = \frac{\tau}{2N} \|D_\tau p^{n+1}\|_{L^2(\Omega)}^2 + \frac{1}{2N} D_\tau \|p^{n+1}\|_{L^2(\Omega)}^2. \quad (14)$$

Substituting Eqs. 12-14 into Eq. 11, we obtain

$$\begin{aligned} & \eta \tau \|\varepsilon(D_\tau \mathbf{u}_s^{n+1})\|_{L^2(\Omega)}^2 + \eta D_\tau \|\varepsilon(\mathbf{u}_s^{n+1})\|_{L^2(\Omega)}^2 \\ &+ \frac{\gamma \tau}{2} \|\nabla \cdot D_\tau \mathbf{u}_s^{n+1}\|_{L^2(\Omega)}^2 + \frac{\gamma}{2} D_\tau \|\nabla \cdot \mathbf{u}_s^{n+1}\|_{L^2(\Omega)}^2 \\ &+ \frac{\tau}{2N} \|D_\tau p^{n+1}\|_{L^2(\Omega)}^2 + \frac{1}{2N} D_\tau \|p^{n+1}\|_{L^2(\Omega)}^2 - (D_\tau \phi^{n+1}, p^{n+1}) \\ &= 0. \end{aligned} \quad (15)$$

By Eq. 15, we have

$$\begin{aligned} & \frac{1}{\tau} (\eta \|\varepsilon(\mathbf{u}_s^{n+1})\|_{L^2(\Omega)}^2 - \eta \|\varepsilon(\mathbf{u}_s^n)\|_{L^2(\Omega)}^2) \\ &+ \frac{\gamma}{2} \|\nabla \cdot \mathbf{u}_s^{n+1}\|_{L^2(\Omega)}^2 - \frac{\gamma}{2} \|\nabla \cdot \mathbf{u}_s^n\|_{L^2(\Omega)}^2 \\ &+ \frac{\tau}{2N} \|p^{n+1}\|_{L^2(\Omega)}^2 - \frac{\tau}{2N} \|p^n\|_{L^2(\Omega)}^2 - (\phi^{n+1} - \phi^n, p^{n+1}) \\ &\leq 0. \end{aligned} \quad (16)$$

According to Eq. 8, we get the dissipation equality of the total energy:

$$\begin{aligned} E^{n+1} - E^n &= \int_{\Omega} (\phi^{n+1} f(c^{n+1}) - \phi^n f(c^n)) dx \\ &+ \eta \|\varepsilon(\mathbf{u}_s^{n+1})\|_{L^2(\Omega)}^2 - \eta \|\varepsilon(\mathbf{u}_s^n)\|_{L^2(\Omega)}^2 \\ &+ \frac{\gamma}{2} \|\nabla \cdot \mathbf{u}_s^{n+1}\|_{L^2(\Omega)}^2 - \frac{\gamma}{2} \|\nabla \cdot \mathbf{u}_s^n\|_{L^2(\Omega)}^2 \\ &+ \frac{1}{2N} \|p^{n+1}\|_{L^2(\Omega)}^2 - \frac{1}{2N} \|p^n\|_{L^2(\Omega)}^2. \end{aligned} \quad (17)$$

Using Eqs. 6b, 6c and 10, we get

$$\begin{aligned} & \tau^{-1} \int_{\Omega} (\phi^{n+1} f(c^{n+1}) - \phi^n f(c^n)) dx + (\phi^{n+1} - \phi^n, p^{n+1}) \\ &\leq \tau^{-1} \int_{\Omega} \mu^{n+1} (\phi^{n+1} c^{n+1} - \phi^n c^n) dx \\ &= - \int_{\Omega} \mu^{n+1} \nabla \cdot (\mathbf{v}_f^{n+1} c^n) dx \\ &= \int_{\Omega} \mathbf{v}_f^{n+1} \cdot c^n \nabla \mu^{n+1} dx \\ &= - \int_{\Omega} \lambda(\phi^n) |c^n \nabla \mu^{n+1}|^2 dx. \end{aligned} \quad (18)$$

Combining Eqs. 16 and 18, we obtain

$$E^{n+1} - E^n \leq 0. \quad (19)$$

The proof is completed. \square

4. Full discretization

This section focuses on the construction of the full discretization based on the finite element methods.

4.1 Discrete formulations

The domain Ω is subdivided by a family of triangulation grids \mathcal{K}_h . We denote the element diameter by h_K , $K \in \mathcal{K}_h$, and denote \mathcal{V}_h as:

$$\mathcal{V}_h := \left\{ \rho \in L^2(\Omega)^d : \rho|_K \in \mathbb{P}_1(K)^d, \forall K \in \mathcal{K}_h \right\}.$$

The set containing all the faces (when $d = 3$) or edges (when $d = 2$) of the mesh \mathcal{K}_h is denoted as \mathcal{E}_h . We use the notation \mathcal{E}_h^l to represent the set of interfaces for \mathcal{E}_h . Let $K_i, K_j \in \mathcal{K}_h$ are two neighboring elements. Then there exists $e = \partial K_i \cap \partial K_j \in \mathcal{E}_h^l$ with the unit outer normal vector \mathbf{n}_e orient from K_i to K_j . The average and jumping values for $\rho \in \mathcal{V}_h$ on e are defined as follows:

$$\{\rho\} := \frac{1}{2}((\rho|_{K_i})|_e + (\rho|_{K_j})|_e), \quad [\rho] := (\rho|_{K_i})|_e - (\rho|_{K_j})|_e,$$

where $\rho|_{K_i}$ represents the value of ρ in K_i . Within any subdomain D of Ω , we denote the inner product of scalar functions ϑ_1 and ϑ_2 by $(\vartheta_1, \vartheta_2)_D = \int_D \vartheta_1 \vartheta_2 dx$, and for vector functions ϑ_1 and ϑ_2 as $(\vartheta_1, \vartheta_2)_D = \int_D \vartheta_1 \cdot \vartheta_2 dx$. We use $\|\cdot\|_{L^2(D)}$ to denote the L^2 -norm on D . For any edge or face e , the inner product on the space $L^2(e)$ is represented by $\langle \cdot, \cdot \rangle_e$ and the corresponding norm is written as $\|\cdot\|_{L^2(e)}$.

We use the upwind strategy to deal with the convection term, the upwind value of c_h^n on the interior edge is expressed as:

$$c_h^{n*} = \begin{cases} c_h^n|_{K_i}, & \mathbf{v}_{f,h}^n \cdot \mathbf{n}_e \geq 0, \\ c_h^n|_{K_j}, & \mathbf{v}_{f,h}^n \cdot \mathbf{n}_e < 0. \end{cases} \quad (20)$$

The lowest-order Raviart-Thomas mixed finite element space is introduced as:

$$\mathcal{U}_h = \{ \mathbf{x}_h \in H(\text{div}, \Omega) : \mathbf{x}_h|_K \in RT_0(K), \forall K \in \mathcal{K}_h \},$$

$$\mathcal{Q}_h = \{ z_h \in L^2(\Omega) : z_h|_K \in \mathbb{P}_0(K), \forall K \in \mathcal{K}_h \},$$

where $H(\text{div}, \Omega) = \{ \mathbf{x} \in [L^2(\Omega)]^d : \nabla \cdot \mathbf{x} \in L^2(\Omega) \}$. Let $\mathcal{U}_h^0 = \{ \mathbf{x} \in \mathcal{U}_h : \mathbf{x} \cdot \mathbf{n} = 0 \text{ on } \partial\Omega \}$.

We define:

$$\begin{aligned} \mathcal{A}(\mathbf{u}_{s,h}, p_h, \mathbf{v}_h) &:= \sum_{K \in \mathcal{K}_h} (\sigma_e(\mathbf{u}_{s,h}), \varepsilon(\mathbf{v}_h))_K - \sum_{e \in \mathcal{E}_h^l} \langle \{ \sigma_e(\mathbf{u}_{s,h}) \mathbf{n}_e \}, [\mathbf{v}_h] \rangle_e \\ &\quad - \alpha \sum_{K \in \mathcal{K}_h} (p_h, \nabla \cdot \mathbf{v}_h)_K + \alpha \sum_{e \in \mathcal{E}_h^l} \langle \{ p_h \mathbf{n}_e \}, [\mathbf{v}_h] \rangle_e \\ &\quad - \sum_{e \in \mathcal{E}_h^l} \langle [\mathbf{u}_{s,h}], \{ \sigma_e(\mathbf{v}_h) \mathbf{n}_e \} \rangle_e + \sum_{e \in \mathcal{E}_h^l} \frac{\theta_e}{h_e} \langle [\mathbf{u}_{s,h}], [\mathbf{v}_h] \rangle_e, \end{aligned}$$

where θ_e denotes a penalty parameter and h_e is determined by $h_e = |e|^{\frac{1}{d-1}}$.

For any $\mathbf{v}_h \in \mathcal{V}_h$, $\mathbf{w}_h \in \mathcal{U}_h^0$, $q_h, z_h, \rho_h \in \mathcal{Q}_h$, we find $\mathbf{u}_{s,h}^{n+1} \in \mathcal{V}_h$, $\mathbf{v}_{f,h}^{n+1} \in \mathcal{U}_h$, $c_h^{n+1}, \phi_h^{n+1}, p_h^{n+1} \in \mathcal{Q}_h$ such that

$$\mathcal{A}(\mathbf{u}_{s,h}^{n+1}, p_h^{n+1}, \mathbf{v}_h) = 0, \quad (21a)$$

$$(D_\tau(\phi_h^{n+1} c_h^{n+1}), q_h) + \sum_{e \in \mathcal{E}_h^l} \langle c_h^{n*} \mathbf{v}_{f,h}^{n+1} \cdot \mathbf{n}, [q_h] \rangle_e = 0, \quad (21b)$$

$$(\lambda^{-1}(\phi_h^{n+1}) \mathbf{v}_{f,h}^{n+1}, \mathbf{w}_h) = \sum_{e \in \mathcal{E}_h^l} \langle [\mu_h^{n+1}], c_h^{n*} \mathbf{w}_h \cdot \mathbf{n} \rangle_e, \quad (21c)$$

$$(p_h^{n+1}, z_h) = (c_h^n \mu_h^{n+1} - f(c_h^n), z_h), \quad (21d)$$

$$\begin{aligned} (D_\tau \phi_h^{n+1}, \rho_h) &= \frac{1}{N} (D_\tau p_h^{n+1}, \rho_h) + \alpha (D_\tau(\nabla \cdot \mathbf{u}_{s,h}^{n+1}), \rho_h) \\ &\quad - \alpha \sum_{e \in \mathcal{E}_h^l} \langle \{ \rho_h \mathbf{n}_e \}, [D_\tau \mathbf{u}_{s,h}^{n+1}] \rangle_e. \end{aligned} \quad (21e)$$

As the scheme in Eqs. 21 leads to a nonlinear system, we use an iterative method to solve Eqs. 21:

$$\mathcal{A}(\mathbf{u}_{s,h}^{n+1,l+1}, p_h^{n+1,l+1}, \mathbf{v}_h) = 0, \quad (22a)$$

$$(D_\tau(\phi_h^{n+1,l} c_h^{n+1,l+1}), q_h) + \sum_{e \in \mathcal{E}_h^l} \langle c_h^{n*} \mathbf{v}_{f,h}^{n+1,l+1} \cdot \mathbf{n}, [q_h] \rangle_e = 0, \quad (22b)$$

$$(\lambda^{-1}(\phi_h^n) \mathbf{v}_{f,h}^{n+1,l+1}, \mathbf{w}_h) = \sum_{e \in \mathcal{E}_h^l} \langle [\mu_h^{n+1,l+1}], c_h^{n*} \mathbf{w}_h \cdot \mathbf{n} \rangle_e, \quad (22c)$$

$$(p_h^{n+1,l+1}, z_h) = (c_h^n \mu_h^{n+1,l+1} - f(c_h^n), z_h), \quad (22d)$$

$$\begin{aligned} (D_\tau \phi_h^{n+1,l+1}, \rho_h) &= \frac{1}{N} (D_\tau p_h^{n+1,l+1}, \rho_h) + \alpha (D_\tau(\nabla \cdot \mathbf{u}_{s,h}^{n+1,l+1}), \rho_h) \\ &\quad - \alpha \sum_{e \in \mathcal{E}_h^l} \langle \{ \rho_h \mathbf{n}_e \}, [D_\tau \mathbf{u}_{s,h}^{n+1,l+1}] \rangle_e, \end{aligned} \quad (22e)$$

where l and $l+1$ represent the iterative steps.

For given c_h^n , $\mathbf{u}_{s,h}^n$, $\mathbf{v}_{f,h}^n$, ϕ_h^n and p_h^n , we choose the initial approximations as $c_h^{n+1,0} = c_h^n$, $\mathbf{u}_{s,h}^{n+1,0} = \mathbf{u}_{s,h}^n$, $\mathbf{v}_{f,h}^{n+1,0} = \mathbf{v}_{f,h}^n$ and $\phi_h^{n+1,0} = \phi_h^n$, $p_h^{n+1,0} = p_h^n$.

4.2 Theoretical analysis

The scheme 21 still inherits the property of energy decay and enjoys the feature that local mass conservation and the conservation of total mass are maintained despite the porosity variations in both space and time.

Theorem 4.1. *The scheme 21 maintains the properties of total mass conservation and local mass conservation:*

$$\sum_{K \in \mathcal{K}_h} |K| \phi_h^{n+1} c_h^{n+1} = \sum_{K \in \mathcal{K}_h} |K| \phi_h^n c_h^n = \dots = \sum_{K \in \mathcal{K}_h} |K| \phi_h^0 c_h^0. \quad (23)$$

Proof. Let $q_h = 1$ in $K \in \mathcal{K}_h$ and $q_h = 0$ in $\mathcal{K}_h \setminus K$ in Eq. 21b, we get

$$|K| \frac{\phi_h^{n+1} c_h^{n+1} - \phi_h^n c_h^n}{\tau} = - \sum_{e \in \partial K} |e| c_h^{n*} \mathbf{v}_{f,h}^{n+1} \cdot \mathbf{n}, \quad (24)$$

which indicates that the scheme 21 enjoys the local mass conservation. Summing Eq. 24 overall control volumes, we deduce that

$$\begin{aligned}
& \sum_{K \in \mathcal{K}_h} |K| \frac{\phi_h^{n+1} c_h^{n+1} - \phi_h^n c_h^n}{\tau} \\
&= - \sum_{K \in \mathcal{K}_h} \sum_{e \in \partial K} |e| c_h^{n*} \mathbf{v}_{f,h}^{n+1} \cdot \mathbf{n} \\
&= - \left(\sum_{e^+ \in \mathcal{E}_h^I} |e| c_h^{n*} \mathbf{v}_{f,h}^{n+1} \cdot \mathbf{n} + \sum_{e^- \in \mathcal{E}_h^I} |e| c_h^{n*} \mathbf{v}_{f,h}^{n+1} \cdot \mathbf{n} \right) \\
&= 0, \tag{25}
\end{aligned}$$

where $e^+ = \{e \in \partial K \cap \partial K_1 : \mathbf{v}_{f,h}^{n+1} \cdot \mathbf{n}|_e > 0, \forall K, K_1 \in \mathcal{K}_h\}$,
 $e^- = \{e \in \partial K_1 \cap \partial K : \mathbf{v}_{f,h}^{n+1} \cdot \mathbf{n}|_e < 0, \forall K, K_1 \in \mathcal{K}_h\}$. \square

We define the energy as follows:

$$\begin{aligned}
E_h^n &= \sum_{e \in \mathcal{E}_h^I} \frac{\theta_e}{2h_e} \langle [\mathbf{u}_{s,h}^n], [\mathbf{u}_{s,h}^n] \rangle_e - \sum_{e \in \mathcal{E}_h^I} \langle \{\sigma_e(\mathbf{u}_{s,h}^n) \mathbf{n}_e\}, [\mathbf{u}_{s,h}^n] \rangle_e \\
&+ \sum_{K \in \mathcal{K}_h} \int_K \left(\phi_h^n f(c_h^n) + \frac{\sigma_e(\mathbf{u}_{s,h}^n) : \varepsilon(\mathbf{u}_{s,h}^n)}{2} + \frac{|p_h^n|^2}{2N} \right) dx. \tag{26}
\end{aligned}$$

Theorem 4.2. Assume that $0 < \varepsilon \leq c_h^n \leq \frac{1}{\beta} - \varepsilon$ where ε is a small constant. The stabilization parameter θ is taken as in Theorem 3.1. The total free energy stemming from the scheme 21 follows the inequality:

$$D_\tau E_h^{n+1} \leq - \sum_{K \in \mathcal{K}_h} \int_K \lambda^{-1} (\phi_h^n) |\mathbf{v}_{f,h}^{n+1}|^2 dx \leq 0.$$

Proof. Taking $\mathbf{v}_h = D_\tau \mathbf{u}_{s,h}$ and $\rho_h = p_h^{n+1}$ in Eqs. 21a and 21e, we have

$$\begin{aligned}
& \frac{1}{2} \sum_{K \in \mathcal{K}_h} D_\tau (\sigma_e(\mathbf{u}_{s,h}^{n+1}), \varepsilon(\mathbf{u}_{s,h}^{n+1}))_K \\
&+ \frac{\tau}{2} \sum_{K \in \mathcal{K}_h} (\sigma_e(D_\tau \mathbf{u}_{s,h}^{n+1}), \varepsilon(D_\tau \mathbf{u}_{s,h}^{n+1}))_K \\
&+ \frac{1}{2N} \sum_{K \in \mathcal{K}_h} D_\tau (p_h^{n+1}, p_h^{n+1})_K + \frac{\tau}{2N} \sum_{K \in \mathcal{K}_h} (D_\tau p_h^{n+1}, D_\tau p_h^{n+1})_K \\
&+ \sum_{e \in \mathcal{E}_h^I} \frac{\theta_e}{2h_e} D_\tau \langle [\mathbf{u}_{s,h}^{n+1}], [\mathbf{u}_{s,h}^{n+1}] \rangle_e + \sum_{e \in \mathcal{E}_h^I} \frac{\theta_e \tau}{2h_e} \langle [D_\tau \mathbf{u}_{s,h}^{n+1}], [D_\tau \mathbf{u}_{s,h}^{n+1}] \rangle_e \\
&- \sum_{e \in \mathcal{E}_h^I} \langle \{\sigma_e(\mathbf{u}_{s,h}^{n+1}) \mathbf{n}_e\}, [D_\tau \mathbf{u}_{s,h}^{n+1}] \rangle_e - \sum_{K \in \mathcal{K}_h} (D_\tau \phi_h^{n+1}, p_h^{n+1})_K \\
&- \sum_{e \in \mathcal{E}_h^I} \langle [\mathbf{u}_{s,h}^{n+1}], \{\sigma(D_\tau \mathbf{u}_{s,h}^{n+1}) \mathbf{n}_e\} \rangle_e = 0. \tag{27}
\end{aligned}$$

Combining the 7th and 8th terms of Eq. 27, we can arrive at the ensuing equality via a simple derivation process:

$$\begin{aligned}
& \langle \{\sigma_e(\mathbf{u}_{s,h}^{n+1}) \mathbf{n}_e\}, [D_\tau \mathbf{u}_{s,h}^{n+1}] \rangle_e + \langle \{\sigma_e(D_\tau \mathbf{u}_{s,h}^{n+1}) \mathbf{n}_e\}, [\mathbf{u}_{s,h}^{n+1}] \rangle_e \\
&= \frac{1}{\tau} (\langle \{\sigma_e(\mathbf{u}_{s,h}^{n+1} - \mathbf{u}_{s,h}^n) \mathbf{n}_e\}, [\mathbf{u}_{s,h}^{n+1} - \mathbf{u}_{s,h}^n] \rangle_e \\
&+ \langle \{\sigma_e(\mathbf{u}_{s,h}^{n+1}) \mathbf{n}_e\}, [\mathbf{u}_{s,h}^{n+1}] \rangle_e - \langle \{\sigma_e(\mathbf{u}_{s,h}^n) \mathbf{n}_e\}, [\mathbf{u}_{s,h}^n] \rangle_e). \tag{28}
\end{aligned}$$

By the Cauchy-Schwarz and Young's inequalities, we get

$$\sum_{e \in \mathcal{E}_h^I} \tau \langle \{\sigma_e(D_\tau \mathbf{u}_{s,h}^{n+1}) \mathbf{n}_e\}, [D_\tau \mathbf{u}_{s,h}^{n+1}] \rangle_e \tag{29}$$

$$\begin{aligned}
& \leq \sum_{e \in \mathcal{E}_h^I} \tau \|\{\sigma_e(D_\tau \mathbf{u}_{s,h}^{n+1}) \mathbf{n}_e\}\|_{L^2(e)} \| [D_\tau \mathbf{u}_{s,h}^{n+1}] \|_{L^2(e)} \\
& \leq \left(\sum_{e \in \mathcal{E}_h^I} \tau \|\{\sigma_e(D_\tau \mathbf{u}_{s,h}^{n+1}) \mathbf{n}_e\}\|_{L^2(e)}^2 \right)^{\frac{1}{2}} \left(\sum_{e \in \mathcal{E}_h^I} \tau \| [D_\tau \mathbf{u}_{s,h}^{n+1}] \|_{L^2(e)}^2 \right)^{\frac{1}{2}} \\
& \leq \left(\frac{C\tau}{2h_e} \sum_{K \in \mathcal{K}_h} (\sigma_e(D_\tau \mathbf{u}_{s,h}^{n+1}), \varepsilon(D_\tau \mathbf{u}_{s,h}^{n+1}))_K \right)^{\frac{1}{2}} \\
& \quad \cdot \left(\sum_{e \in \mathcal{E}_h^I} \tau \| [D_\tau \mathbf{u}_{s,h}^{n+1}] \|_{L^2(e)}^2 \right)^{\frac{1}{2}} \\
& \leq \frac{\tau}{4} \sum_{K \in \mathcal{K}_h} (\sigma_e(D_\tau \mathbf{u}_{s,h}^{n+1}), \varepsilon(D_\tau \mathbf{u}_{s,h}^{n+1}))_K \\
& \quad + \frac{C\tau}{2h_e} \sum_{e \in \mathcal{E}_h^I} \| [D_\tau \mathbf{u}_{s,h}^{n+1}] \|_{L^2(e)}^2.
\end{aligned}$$

This derivation employs the trace inequality (cf. [34]):

$$\|\sigma_e(\mathbf{v}_h) \mathbf{n}\|_{L^2(e)}^2 \leq Ch_e^{-1} \int_K (\sigma_e(\mathbf{v}_h) : \varepsilon(\mathbf{v}_h)) dx, \quad \forall \mathbf{v}_h \in \mathbb{P}_r(K)^d, \tag{30}$$

where \mathbb{P}_r is the r th-order polynomial space.

Substituting Eqs. 28 and 29 into Eq. 27, we get

$$\begin{aligned}
& \frac{1}{2} \sum_{K \in \mathcal{K}_h} D_\tau (\sigma_e(\mathbf{u}_{s,h}^{n+1}), \varepsilon(\mathbf{u}_{s,h}^{n+1}))_K \\
&+ \frac{\tau}{4} \sum_{K \in \mathcal{K}_h} (\sigma_e(D_\tau \mathbf{u}_{s,h}^{n+1}), \varepsilon(D_\tau \mathbf{u}_{s,h}^{n+1}))_K \\
&+ \frac{1}{2N} \sum_{K \in \mathcal{K}_h} D_\tau (p_h^{n+1}, p_h^{n+1})_K + \frac{\tau}{2N} \sum_{K \in \mathcal{K}_h} (D_\tau p_h^{n+1}, D_\tau p_h^{n+1})_K \\
&+ \sum_{e \in \mathcal{E}_h^I} \frac{\theta_e}{2h_e} D_\tau \langle [\mathbf{u}_{s,h}^{n+1}], [\mathbf{u}_{s,h}^{n+1}] \rangle_e \\
&+ \sum_{e \in \mathcal{E}_h^I} \frac{(\theta_e - C)\tau}{2h_e} \langle [D_\tau \mathbf{u}_{s,h}^{n+1}], [D_\tau \mathbf{u}_{s,h}^{n+1}] \rangle_e \\
&- \sum_{e \in \mathcal{E}_h^I} \langle \{\sigma_e(\mathbf{u}_{s,h}^{n+1}) \mathbf{n}_e\}, [\mathbf{u}_{s,h}^{n+1}] \rangle_e \\
&+ \sum_{e \in \mathcal{E}_h^I} \langle \{\sigma_e(\mathbf{u}_{s,h}^n) \mathbf{n}_e\}, [\mathbf{u}_{s,h}^n] \rangle_e - \sum_{K \in \mathcal{K}_h} (D_\tau \phi_h^{n+1}, p_h^{n+1})_K \\
&\leq 0. \tag{31}
\end{aligned}$$

Let $q_h = \mu_h^{n+1}$, $\mathbf{w}_h = \mathbf{v}_{f,h}^{n+1}$ and $z_h = \phi_h^{n+1} - \phi_h^n$ in Eqs. 21b-21d, we get

$$\left(\frac{\phi_h^{n+1} c_h^{n+1} - \phi_h^n c_h^n}{\tau}, \mu_h^{n+1} \right) + \sum_{e \in \mathcal{E}_h^I} \langle c_h^{n*} \mathbf{v}_{f,h}^{n+1} \cdot \mathbf{n}, \mu_h^{n+1} \rangle_e = 0, \tag{32}$$

$$(\lambda^{-1} (\phi_h^n) \mathbf{v}_{f,h}^{n+1}, \mathbf{v}_{f,h}^{n+1}) = \sum_{e \in \mathcal{E}_h^I} \langle \mu_h^{n+1}, c_h^{n*} \mathbf{v}_{f,h}^{n+1} \cdot \mathbf{n} \rangle_e, \tag{33}$$

$$(p_h^{n+1}, \phi_h^{n+1} - \phi_h^n) = (c_h^n \mu_h^{n+1} - f(c_h^n), \phi_h^{n+1} - \phi_h^n). \tag{34}$$

By Eqs. 9, 10 and 32-34, we can get the following results:

$$\begin{aligned}
& \frac{1}{\tau} \sum_{K \in \mathcal{K}_h} \int_K \mu_h^{n+1} (\phi_h^{n+1} c_h^{n+1} - \phi_h^n c_h^n) dx \\
&= - \sum_{e \in \mathcal{E}_h^I} \int_e [\mu_h^{n+1}] c_h^{n*} \mathbf{v}_{f,h}^{n+1} \cdot \mathbf{n} dx \tag{35}
\end{aligned}$$

$$= - \sum_{K \in \mathcal{K}_h} \int_K \lambda^{-1} (\phi_h^n) |\mathbf{v}_{f,h}^{n+1}|^2 dx.$$

Due to Eqs. 31-35, we have

$$D_\tau E_h^{n+1} \leq - \sum_{K \in \mathcal{K}_h} \int_K \lambda^{-1} (\phi_h^n) |\mathbf{v}_{f,h}^{n+1}|^2 dx \leq 0.$$

The proof is completed. \square

5. Numerical examples

This section presents a series of numerical results to validate the theoretical findings. The gas considered here is methane and the relevant physical data is found in Table 1. In all numerical examples, we take $\theta = 1$. The viscosity $\eta = 10^{-5} \text{Pa} \cdot \text{s}$. The two-dimensional cases are defined on the square domain $\Omega = [0, L]^2$, where $L = 100 \text{ m}$. A quasi-uniform 100×100 triangular mesh is used to divide the domain.

Convergence of the iterative process is controlled by the following stopping criterion:

$$\max \left\{ \frac{\|c_h^{n+1,l+1} - c_h^{n+1,l}\|}{\|c_h^n\|}, \frac{\|p_h^{n+1,l+1} - p_h^{n+1,l}\|}{\|p_h^n\|}, \frac{\|\phi_h^{n+1,l+1} - \phi_h^{n+1,l}\|}{\|\phi_h^n\|}, \frac{\|\mathbf{u}_{s,h}^{n+1,l+1} - \mathbf{u}_{s,h}^{n+1,l}\|}{\|\mathbf{u}_{s,h}^n\|}, \frac{\|\mathbf{v}_{f,h}^{n+1,l+1} - \mathbf{v}_{f,h}^{n+1,l}\|}{\|\mathbf{v}_{f,h}^n\|} \right\} < \varepsilon_1.$$

The iterative algorithm employs a convergence criterion based on the tolerance of the relative error, ε_1 , which is set to 5×10^{-13} to ensure sufficiently accurate solutions in all examples.

5.1 Example 1

To verify the effectiveness of the proposed scheme, we simulate a closed system with the molar density and permeability initially specified as:

$$c^0 = c_0 + \text{rand}(x) \cdot (c_1 - c_0),$$

$$k^0 = k_0 + \text{rand}(x) \cdot (k_1 - k_0),$$

where $c_0 = 100 \text{ mol/m}^3$, $c_1 = 300 \text{ mol/m}^3$, $k_0 = 0.5 \text{ md}$, $k_1 = 2 \text{ md}$, and the random function $\text{rand}(x)$ generates a real value between 0 and 1. The reference porosity is taken as $\phi_r = 0.05$. The initial porosity $\phi^0 = \phi_r$. For the time discretization, the time step size is set as $\tau = 36$ seconds.

The results presented in Fig.1 confirm that the proposed scheme upholds the energy decay property, the mass conservation, and the molar density boundedness.

Figs. 2, 3 and 4 depict the distributions of molar density, pressure, and chemical potential at various time instants. It can be seen that the molar density gradually reaches the equilibrium state driven by the chemical potential energy. Fig. 5 illustrates how porosity is influenced by pressure and solid deformation, using the specified parameter values of $N = 10^{10} \text{ Pa}$, $\gamma = 10^9 \text{ Pa}$, and $\eta = 2 \times 10^9 \text{ Pa}$.

5.2 Example 2

This example demonstrates the simulation of a gas flow problem in a reservoir with four channel zones denoted as Ω_l , where the porosity and permeability of the channel zones are respectively $\phi_0 = 0.5$ and $\kappa_0 = 1000 \text{ md}$.

$$\Omega_l = \{x = (x, y) : x \in [0, 100], y \in [20, 22] \cup [38, 40] \cup [58, 60] \cup [78, 80]\}.$$

As depicted in Fig. 6, the initial states of the porosity and permeability are presented. In the area outside the channels, we take the porosity as $\phi^0 = 0.1$, and the permeability is $\kappa^0 = 1 \text{ md}$. The initial porosity is treated as the reference porosity. We take the initial molar density of the entire area as $c^0 = 20 \text{ mol/m}^3$. In this example, we aim to test an open system, so the Dirichlet boundary conditions are applied, with the left boundary set to $c = 200 \text{ mol/m}^3$ and the right boundary set to $c = 20 \text{ mol/m}^3$. The time step size is set to $\tau = 36$ seconds.

Figs. 7, 8, and 9 present the spatial distributions of molar density, chemical potential, and pressure at various time steps. Since the densities are different on boundaries, there is a gradient difference in chemical potential energy between the left and right sides, which drives the molar density to change the higher left-side value to the lower right-side value across the domain. Because the permeability in the channels is larger than that in the surrounding porous media, the density and pressure change faster in the channels. The changes in porosity and permeability over time are shown in Figs. 10 and 11. It can be observed that the changes in porosity and permeability are also more dramatic where the pressure changes drastically.

5.3 Example 3

The gas flow simulation is carried out in a three-dimensional (3D) cubic domain $\Omega = [0, L]^3$, where the length L of each side is 30 meters. The initial porosity and permeability are set to $\phi^0 = 0.2$ and $\kappa^0 = 100 \text{ md}$ in Ω_h respectively, where

$$\Omega_h = \{\mathbf{x} = (x, y, z) : 0.4L < x < 0.6L, 0.4L < y < 0.6L, 0 < z < 0.8L\}.$$

The initial porosity and permeability in the remaining subdomains are $\phi^0 = 0.1$ and $\kappa^0 = 1 \text{ md}$. The initial molar density of the entire area is $c^0 = 50 \text{ mol/m}^3$. We take the bottom of Ω as the Dirichlet boundary conditions with the constant molar density 200 mol/m^3 . The remaining boundaries are no-flow boundaries. The initial porosity and molar density distributions are presented in Fig. 12. A uniform tetrahedron mesh with 27,000 elements is used for the spatial discretization, and the time step size is $\tau = 20$ seconds.

Fig. 13 shows that the molar density flows into the area from the bottom and changes more obviously in the high permeability region. Figs. 14 and 15 show the changes of chemical potential energy and pressure. Figs. 16 and 17 illustrate how the changes in pressure and solid deformation affect porosity and permeability. The change in porosity in the high permeability area is more obvious due to the drastic change

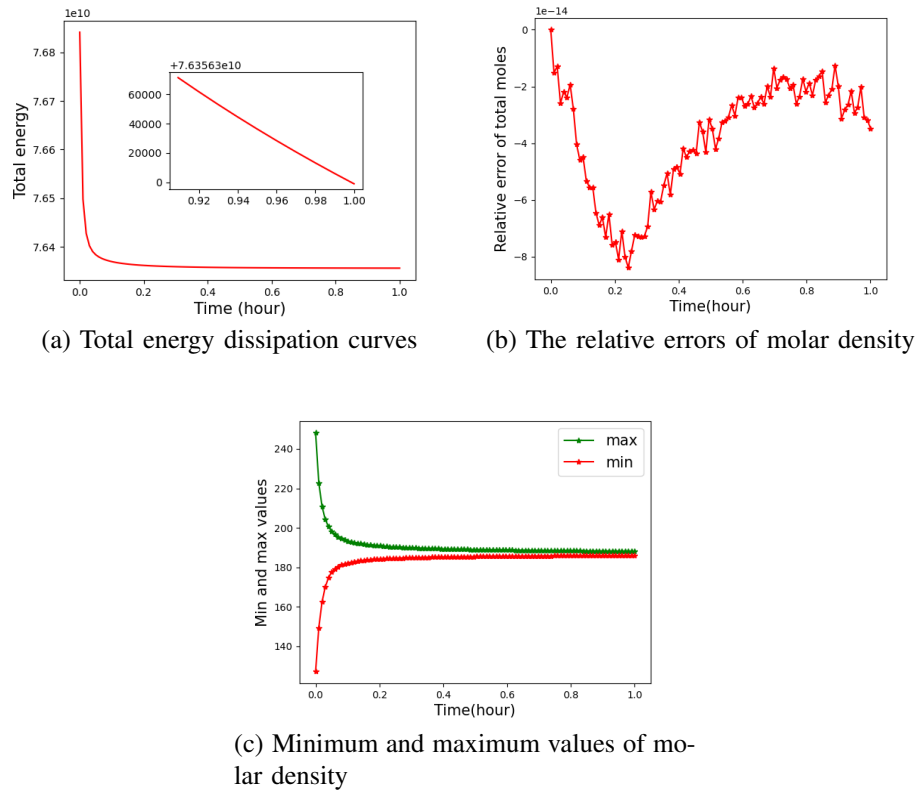


Fig. 1. The performance of the scheme in Example 1.

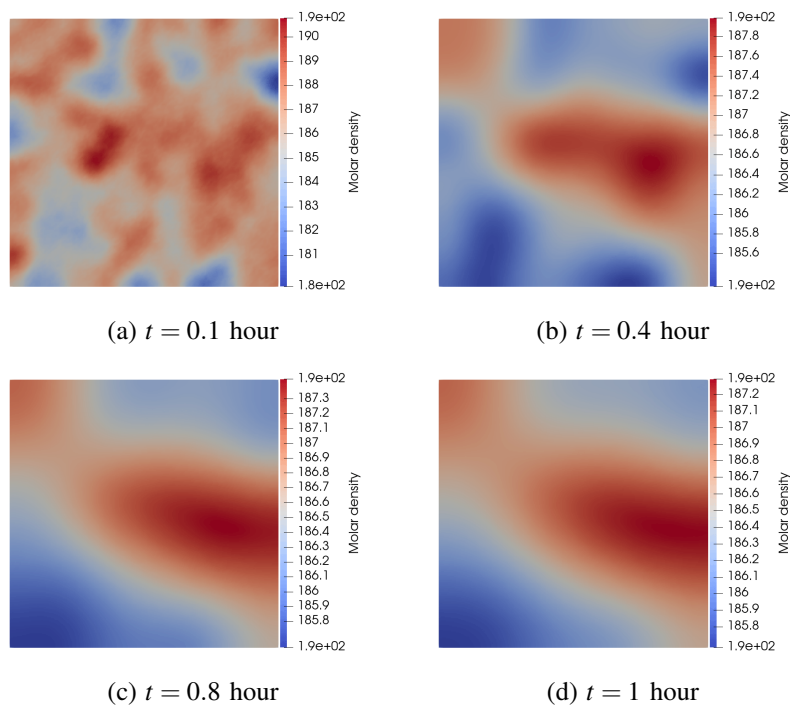
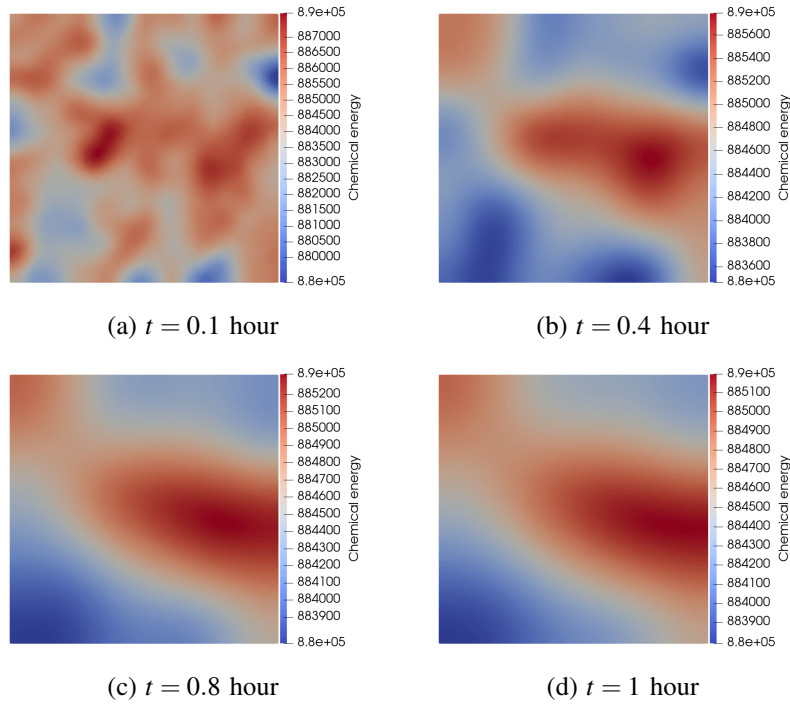
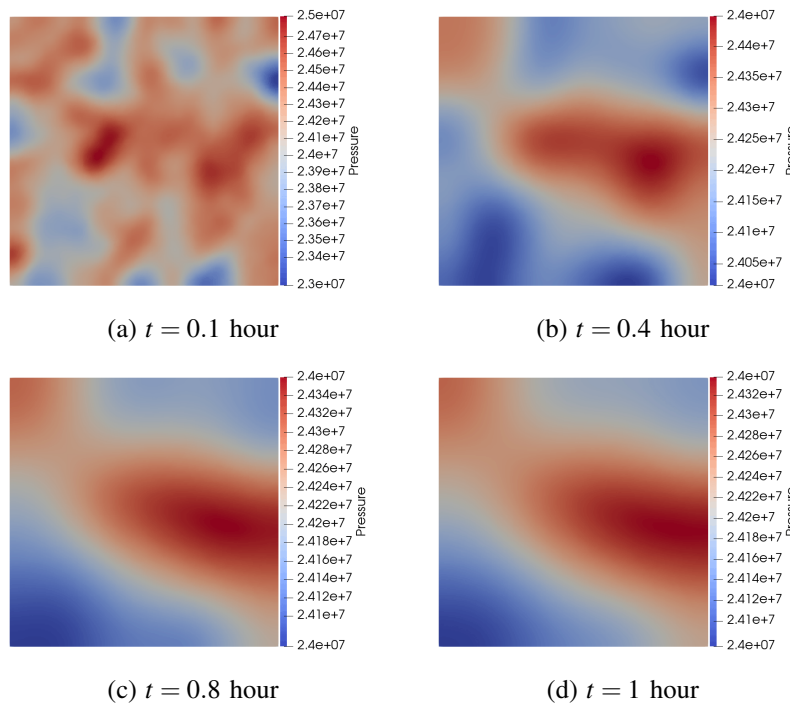


Fig. 2. The molar density distributions at distinct time instants in Example 1.

Table 1. Physical properties of methane.

P_c (bar)	T_c (K)	Acentric factor	M_w (g/mole)	Temperature (K)
45.99	190.56	0.011	16.04	330

**Fig. 3.** The chemical potential distributions at distinct time instants in Example 1.**Fig. 4.** The pressure distributions at distinct time instants in Example 1.

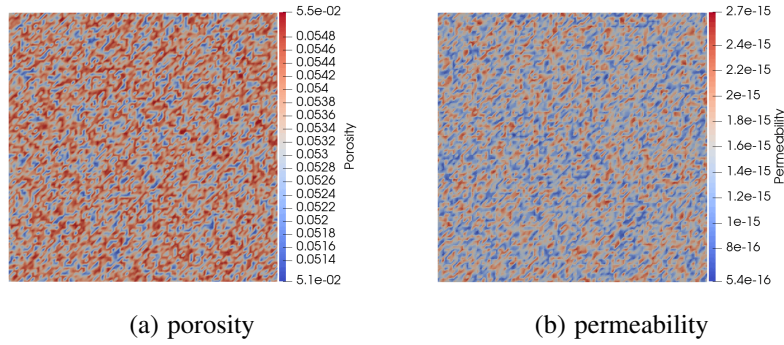


Fig. 5. The porosity and permeability distributions at the final time in Example 1.

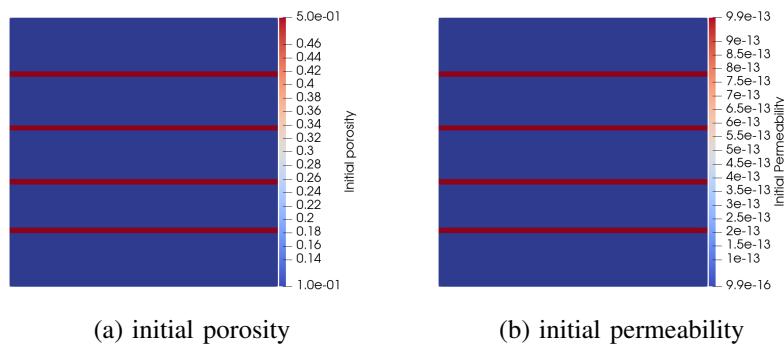


Fig. 6. The initial porosity and permeability distributions in Example 2.

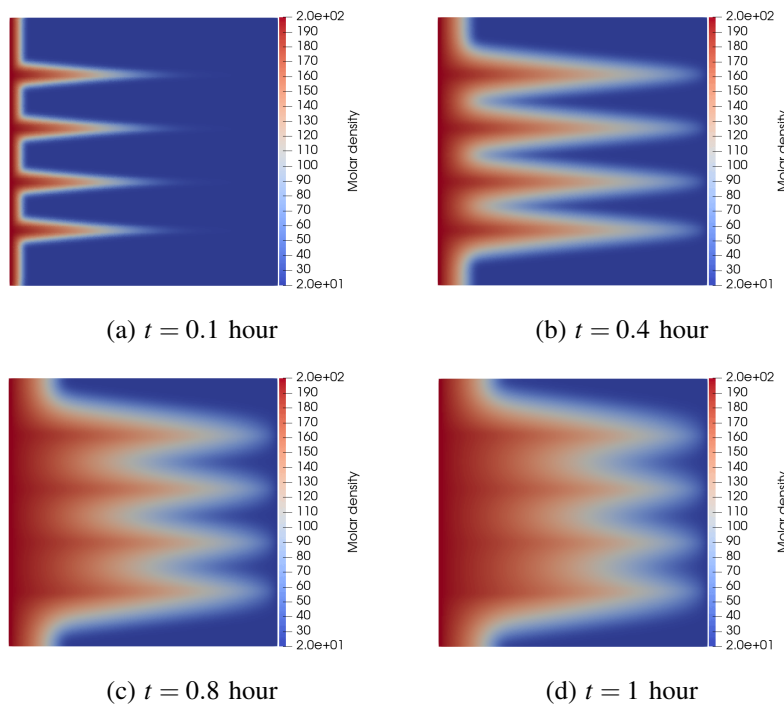


Fig. 7. The molar density distributions at distinct time instants in Example 2.

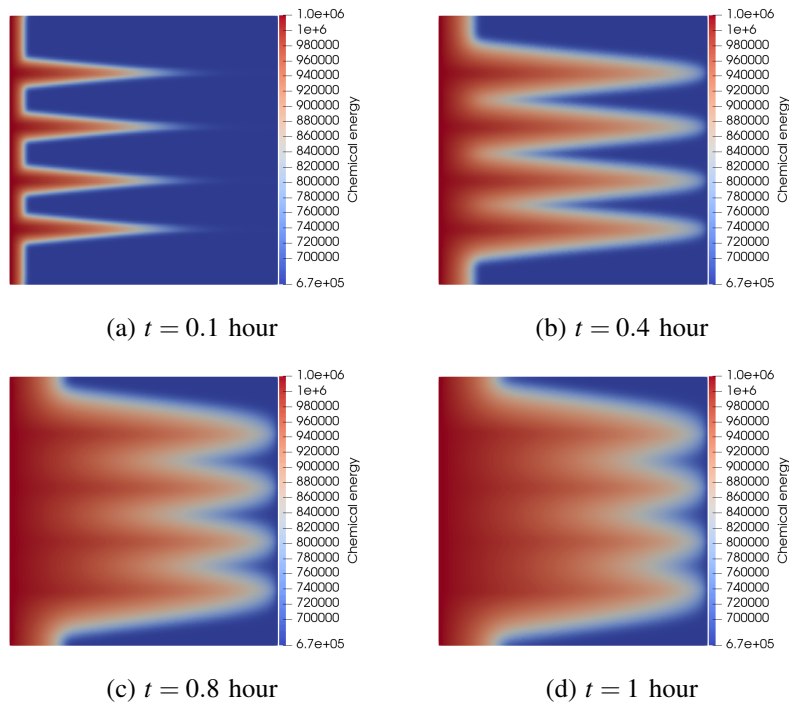


Fig. 8. The chemical potential distributions at distinct time instants in Example 2.

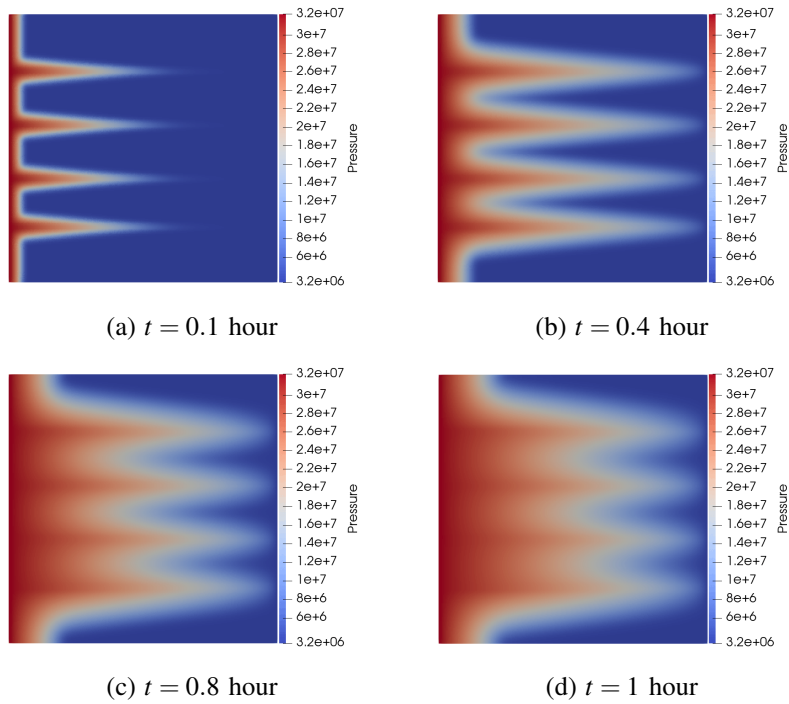


Fig. 9. The pressure distributions at distinct time instants in Example 2.

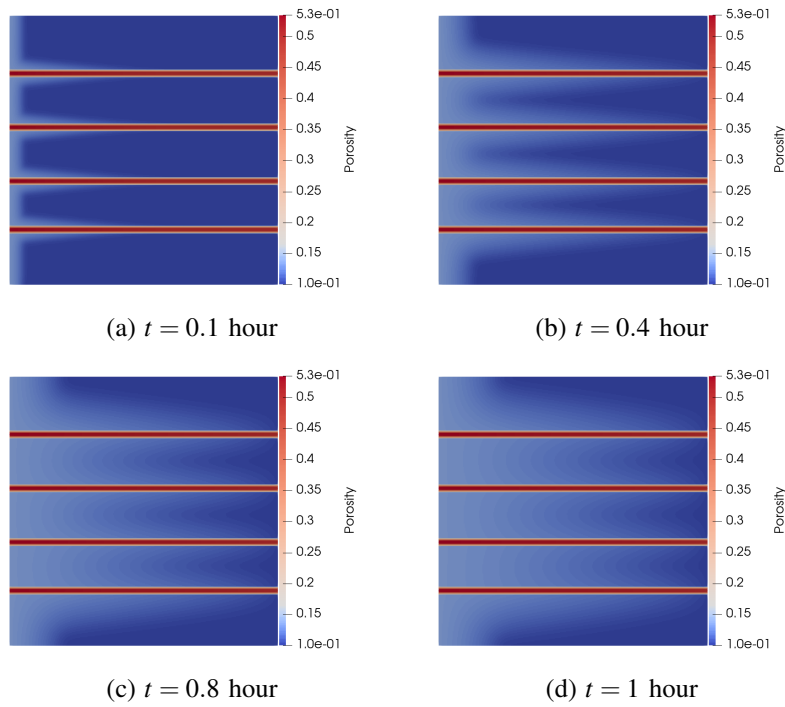


Fig. 10. The porosity distributions at distinct time instants in Example 2.

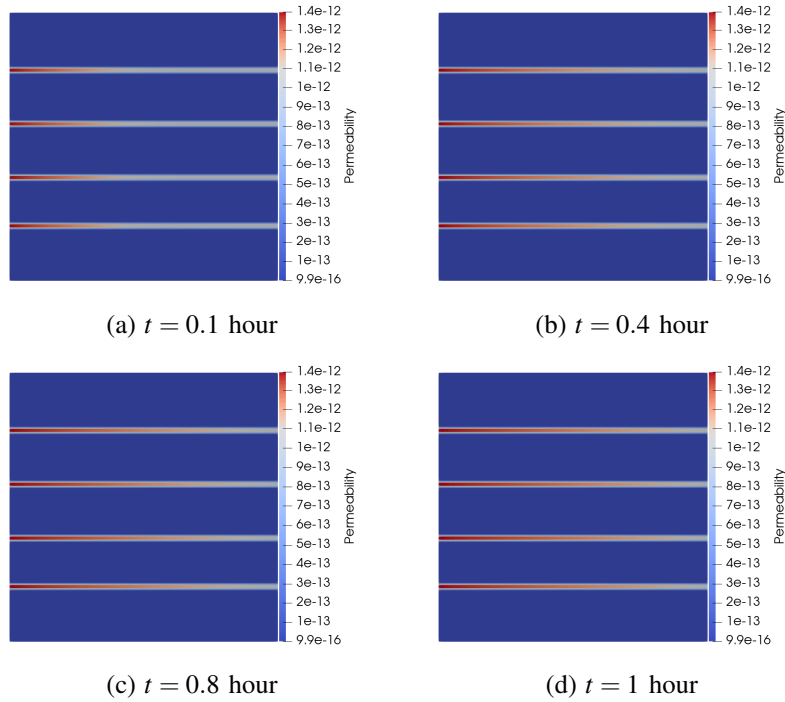


Fig. 11. The permeability distributions at distinct time instants in Example 2.

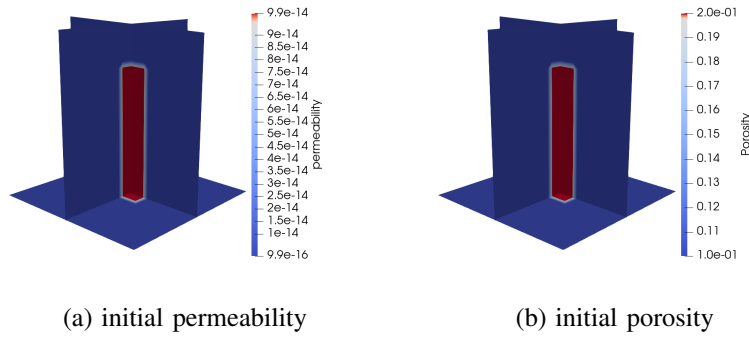


Fig. 12. Initial porosity and permeability in Example 3.

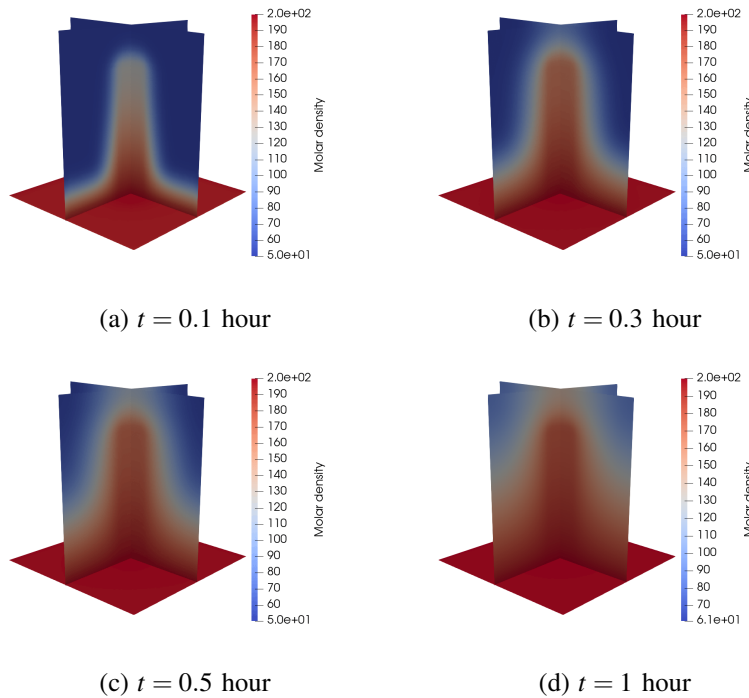


Fig. 13. The molar density distributions at distinct time instants in Example 3.

in pressure. The numerical results confirm that the proposed scheme is a viable and effective approach for simulating the gas flow dynamics in three dimensions.

6. Conclusion

We first introduce an efficient time semi-discrete formulation that employs a stabilization approach, and we subsequently formulate a fully discrete scheme using the mixed finite element and discontinuous Galerkin methods with the upwind strategy. The method ensures the energy dissipation law and the mass conservation law. Numerical results are presented to illustrate the efficiency of the developed numerical scheme.

Acknowledgements

The work was supported by National Key Research and Development Project of China (Grant Number:

2023YFA1011702), and National Natural Science Foundation of China (Grant Number: 12122115).

Conflict of interest

The authors declare no competing interest.

Open Access This article is distributed under the terms and conditions of the Creative Commons Attribution (CC BY-NC-ND) license, which permits unrestricted use, distribution, and reproduction in any medium, provided the original work is properly cited.

References

- Abels, H., Garcke, H., Grün, G. Thermodynamically consistent, frame indifferent diffuse interface models for incompressible two-phase flows with different densities. *Mathematical Models and Methods in Applied Sciences*, 2012, 22(3): 1150013.
- Aki, G. L., Dreyer, W., Giesselmann, J., et al. A quasi-

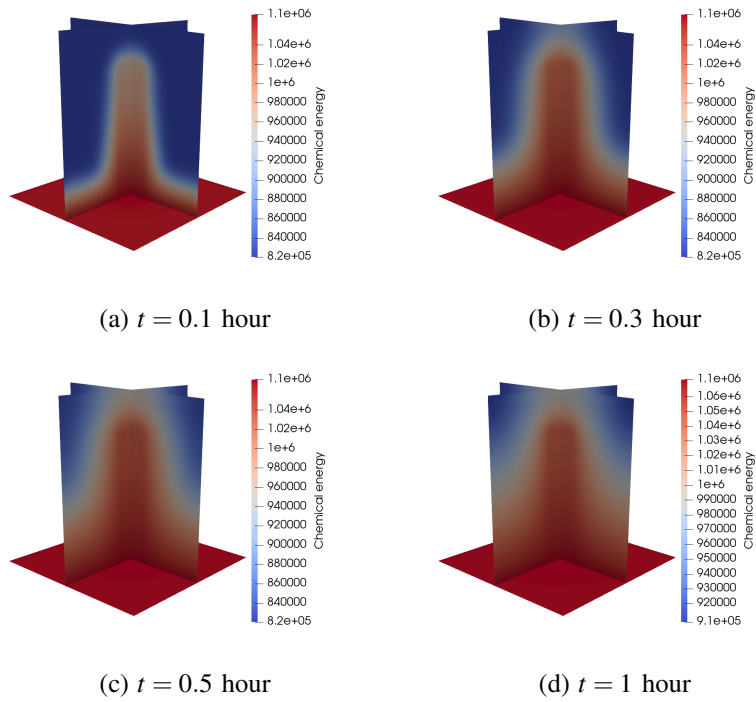


Fig. 14. The chemical energy distributions at distinct time instants in Example 3.

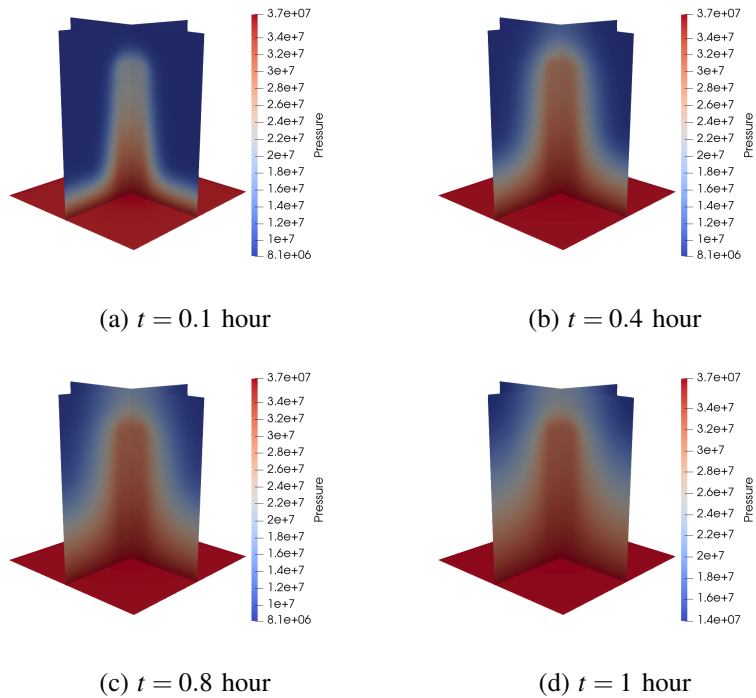


Fig. 15. The pressure distributions at distinct time instants in Example 3.

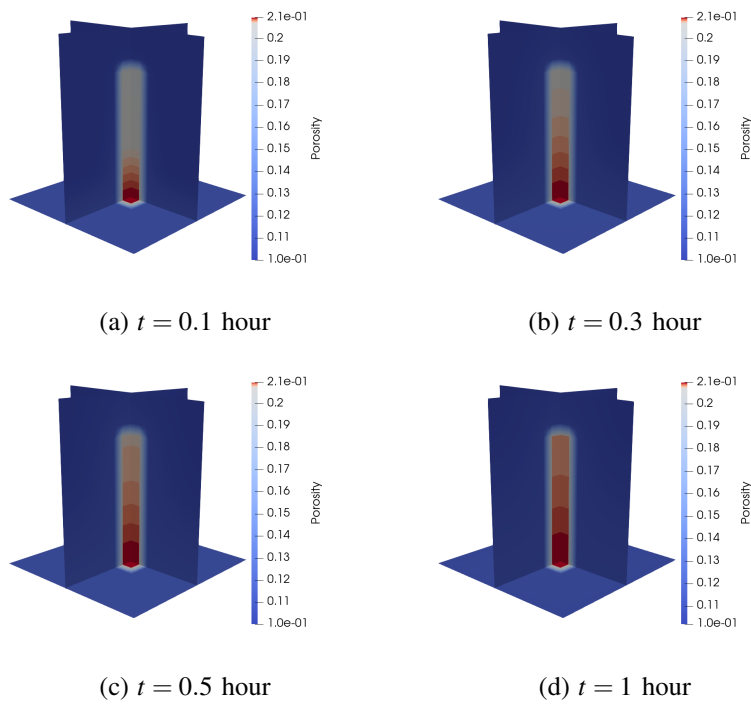


Fig. 16. The porosity distributions at distinct time instants in Example 3.

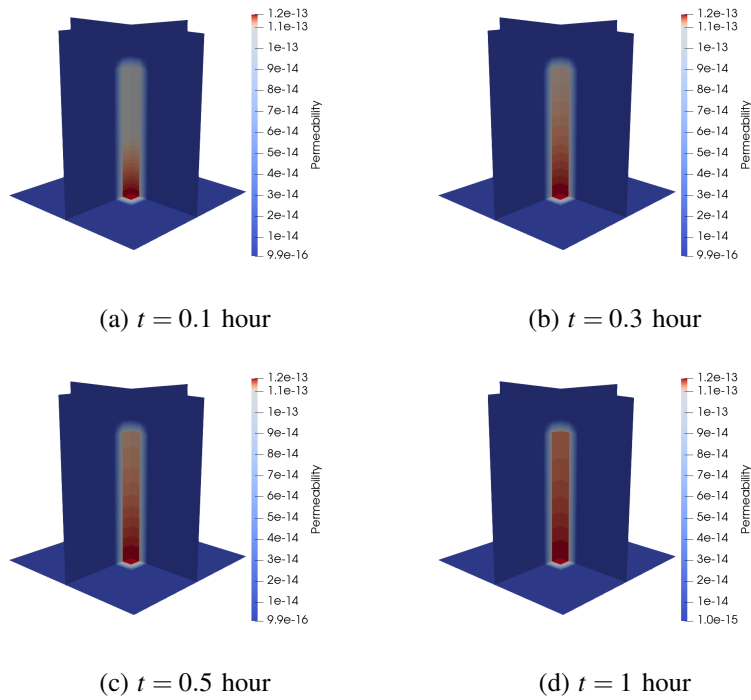


Fig. 17. The permeability distributions at distinct time instants in Example 3.

- incompressible diffuse interface model with phase transition. *Mathematical Models and Methods in Applied Sciences*, 2014, 24(5): 827-861.
- Aland, S., Voigt, A. Benchmark computations of diffuse interface models for two-dimensional bubble dynamics. *International Journal for Numerical Methods in Fluids*, 2012, 69(3): 747-761.
- Abda, A. S., Elhafyana, E., Siddiquia, A. R., et al. A review of the phenomenon of counter-current spontaneous imbibition: Analysis and data interpretation. *Journal of Petroleum Science and Engineering*, 2019d, 180: 456-470.
- Coussy, O. *Poromechanics*. England, John Wiley & sons, 2004.
- Chen, Z., Huan, G., Ma, Y. *Computational methods for multiphase flows in porous media*. Society for Industrial and Applied Mathematics, 2006.
- Chen, H., Kou, J., Sun, S., et al. Fully mass-conservative IMPES schemes for incompressible two-phase flow in porous media. *Computer Methods in Applied Mechanics and Engineering*, 2019, 350: 641-663.
- Chen H., Chen Y., Kou J. Energy stable finite element approximations of gas flow in poroelastic media. *Computer Methods in Applied Mechanics and Engineering*, 2024, 428: 117082.
- Du, Q., Ju, L., Li, X., et al. Maximum bound principles for a class of semilinear parabolic equations and exponential time-differencing schemes. *SIAM review*, 2021, 63(2): 317-359.
- Du, X., Li, Q., Xian, Y., et al. Fully implicit and fully coupled numerical scheme for discrete fracture modeling of shale gas flow in deformable rock. *Journal of Petroleum Science and Engineering*, 2021, 205: 108848.
- Ding, H., Yuan, C. J. On the diffuse interface method using a dual-resolution Cartesian grid. *Journal of Computational Physics*, 2014, 273: 243-254.
- El-Amin, M. F., Kou, J., Sun, S. Mixed finite element simulation with stability analysis for gas transport in low-permeability reservoirs. *Energies*, 2018, 11(1): 208.
- Eyre, D. J. Unconditionally gradient stable time marching the Cahn-Hilliard equation, in *Computational and Mathematical Models of Microstructural Evolution* (San Francisco, CA, 1998). *Mater. Res. Soc. Sympos. Proc.* 529, MRS, Warrendale, PA, 1998: 39-46.
- Firoozabadi, A. *Thermodynamics of hydrocarbon reservoirs*. New York, McGraw-Hill, 1999.
- Guo, C., Bai, B., Wei, M., et al. Study on gas permeability in nano pores of shale gas reservoirs. Paper SPE 167179 Presented at SPE Canada Unconventional Resources Conference, Calgary, Alberta, Canada, 5-7 November, 2013.
- Guo, Z., Lin, P., Lowengrub, J., et al. Mass conservative and energy stable finite difference methods for the quasi-incompressible Navier-Stokes-Cahn-Hilliard system: Primitive variable and projection-type schemes. *Computer Methods in Applied Mechanics and Engineering*, 2017, 326L: 144-174.
- Kou, J., Sun, S. Numerical methods for a multicomponent two-phase interface model with geometric mean influence parameters. *SIAM Journal on Scientific Computing*, 2015, 37(4): B543-B569.
- Kou, J., Sun, S. Thermodynamically consistent modeling and simulation of multi-component two-phase flow with partial miscibility. *Computer Methods in Applied Mechanics and Engineering*, 2018, 331: 623-649.
- Kou, J., Sun, S. Entropy stable modeling of non-isothermal multi-component diffuse-interface two-phase flows with realistic equations of state. *Computer Methods in Applied Mechanics and Engineering*, 2018a, 341: 221-248.
- Kou, J., Wang, X., Zeng, M., et al. Energy stable and mass conservative numerical method for a generalized hydrodynamic phase-field model with different densities. *Physics of Fluids*, 2020, 32(11): 117103.
- Kou, J., Sun, S., Wang, X. A novel energy factorization approach for the diffuse-interface model with Peng-Robinson equation of state. *SIAM Journal on Scientific Computing*, 2020a, 42(1): B30-B56.
- Kou, J., Wang, X., Du, S. Energy stable and mass conservative numerical method for gas flow in porous media with rock compressibility. *SIAM Journal on Scientific Computing*, 2022, 44(4): B938-B963.
- Kou, J., Wang, X., Chen, H., et al. An efficient bound-preserving and energy stable algorithm for compressible gas flow in porous media. *Journal of Computational Physics*, 2023, 473: 111751.
- Lebon, G., Jou, D., Casas-Vázquez, J. *Understanding non-equilibrium thermodynamics*. Springer-Verlag, Berlin Heidelberg, 2008.
- Lowengrub, J., Truskinovsky, L. Quasi-incompressible Cahn-Hilliard fluids and topological transitions. *Proceedings of the Royal Society of London. Series A: Mathematical, Physical and Engineering Sciences*, 1998, 454(1978): 2617-2654.
- Polívka, O., Mikyška, J. Compositional modeling in porous media using constant volume flash and flux computation without the need for phase identification. *Journal of Computational Physics*, 2014, 272: 149-169.
- Peng, D. Y., Robinson, D. B. A new two-constant equation of state. *Industrial & Engineering Chemistry Fundamentals*, 1976, 15(1): 59-64.
- Qiao, Z., Sun, S. Two-phase fluid simulation using a diffuse interface model with Peng-Robinson equation of state. *SIAM Journal on Scientific Computing*, 2014, 36(4): B708-B728.
- Shokrpour Roudbari, M., Şimşek, G., van Brummelen, E. H., et al. Diffuse-interface two-phase flow models with different densities: A new quasi-incompressible form and a linear energy-stable method. *Mathematical Models and Methods in Applied Sciences*, 2018, 28(4): 733-770.
- Shen, J., Yang, X., Wang, Q. Mass and volume conservation in phase field models for binary fluids. *Communications in Computational Physics*, 2013, 13(4): 1045-1065.
- Shen, J., Xu, J., Yang, J. The scalar auxiliary variable (SAV) approach for gradient flows. *Journal of Computational Physics*, 2018, 353: 407-416.
- Shen, J., Xu, J., Yang, J. A new class of efficient and robust

- energy stable schemes for gradient flows. *SIAM Review*, 2019, 61(3): 474-506.
- Wang, Y., Shu, C., Shao, J. Y., et al. A mass-conserved diffuse interface method and its application for incompressible multiphase flows with large density ratio. *Journal of Computational Physics*, 2015, 290: 336-351.
- Schwab, C. *p- and hp-finite element methods: Theory and applications in solid and fluid mechanics*. New York, The Clarendon Press, Oxford University Press, 1998.
- Xu, C., Li, P., Lu, Z., et al. Discrete fracture modeling of shale gas flow considering rock deformation. *Journal of Natural Gas Science and Engineering*, 2018, 52: 507-514.
- Xu, C., Tang, T. Stability analysis of large time-stepping methods for epitaxial growth models. *SIAM Journal on Numerical Analysis*, 2006, 44(4): 1759-1779.
- Yang, X., Ju, L. Efficient linear schemes with unconditional energy stability for the phase field elastic bending energy model. *Computer Methods in Applied Mechanics and Engineering*, 2017, 315: 691-712.
- Yang, X., Zhao, J., Wang, Q. Numerical approximations for the molecular beam epitaxial growth model based on the invariant energy quadratization method. *Journal of Computational Physics*, 2017a, 333: 104-127.
- Yue, P., Zhou, C., Feng, J. J. Spontaneous shrinkage of drops and mass conservation in phase-field simulations. *Journal of Computational Physics*, 2007, 223(1): 1-9.
- Zhu, G., Kou, J., Yao, B., et al. Thermodynamically consistent modelling of two-phase flows with moving contact line and soluble surfactants. *Journal of Fluid Mechanics*, 2019, 879: 327-359.